

Emergence of topological semimetals in gap closing in semiconductors without inversion symmetry

Shuichi Murakami,^{1,2} Motoaki Hirayama,^{1,2} Ryo Okugawa,¹ and Takashi Miyake³

¹*Department of Physics, Tokyo Institute of Technology,
2-12-1 Ookayama, Meguro-ku, Tokyo 152-8551, Japan*

²*TIES, Tokyo Institute of Technology, 2-12-1 Ookayama, Meguro-ku, Tokyo 152-8551, Japan*

³*Research Center for Computational Design of Advanced Functional Materials, AIST, Tsukuba 305-8568, Japan*
(Dated: October 25, 2016)

A band gap for electronic states in crystals governs various properties of solids, such as transport, optical and magnetic properties. Its estimation and control have been an important issue in solid state physics. The band gap can be controlled externally by various parameters, such as pressure, atomic compositions and external field. Sometimes, the gap even collapses by tuning some parameter. In the field of topological insulators, such closing of the gap at a time-reversal invariant momentum indicates a band inversion, i.e. it leads to a topological phase transition from a normal insulator to a topological insulator. Here we show that the gap closing in inversion-asymmetric crystals is universal, in the sense that the gap closing always leads either to a Weyl semimetal or a nodal-line semimetal, from an exhaustive study on possible space groups. We here consider three-dimensional spinful systems with time-reversal symmetry. The space group of the system and the wavevector at the gap closing uniquely determine which possibility occurs and where the gap-closing points or lines lie in the wavevector space after closing of the gap. In particular, we show that an insulator-to-insulator transition never happens, which is in sharp contrast with inversion-symmetric systems.

In electronic band theory of crystals, degeneracy at each wavevector \mathbf{k} is understood in terms of symmetry. A dimension of an irreducible representation of a k -group at a given \mathbf{k} point is equal to degeneracy at the \mathbf{k} point considered. For example, fourfold degeneracy of valence bands at the Γ point in cubic semiconductors comes from cubic symmetry. Meanwhile, proposals of topological semimetals have shown us other possibilities for band degeneracies, stemming from topology. In such a topological semimetal, a band gap closes at generic \mathbf{k} points, and this closing of the gap originates not from symmetry, but from topological reasons. There are various topological semimetals, such as Weyl, Dirac, and nodal-line semimetals. In Weyl semimetals [1–4], the band structure have three-dimensional non-degenerate Dirac cones. There are various proposals of materials for Weyl semimetals [2, 5–12], some of which have been experimentally confirmed such as TaAs [13–15]. Because of topological properties of Weyl nodes [1, 16, 17], characteristic surface states called Fermi arcs arise [2, 18–20]. As another example of topological semimetals, a nodal-line semimetal [22–34] has line nodes along which the band gap closes. Because emergence of topological degeneracy is accidental, search for candidate materials realizing topological semimetals is still elusive.

In the present paper, we consider physics of topological semimetals from a new perspective. Here, we focus on evolution of a band structure of a general inversion-asymmetric insulator by changing a single parameter m , which can be any parameter in the Hamiltonian. We suppose that the gap closes at some value of the parameter m . We then prove that after a further change of the value of m (Fig. 1 a), the system always becomes either (A) a nodal-line semimetal (Fig. 1 b) or (B) a Weyl semimetal (Fig. 1 c). We show that the space group of the crystal and the wavevector at the gap-closing uniquely determines which possibility is realized and where the gap-closing points or lines are located after the closing of the gap.

Here, we restrict ourselves to three-dimensional (3D) spinful systems with time-reversal symmetry, i.e. nonmagnetic systems with nonzero spin-orbit coupling (SOC). In particular, we find that an insulator-to-insulator (ITI) phase transition never occurs in any inversion asymmetric systems. It is in sharp contrast with inversion-symmetric systems.

This work is motivated by the universal phase diagram (Fig. 2a) between a topological insulator (TI) and a normal insulator (NI) in three dimensions [1]. Our result in the present paper indicates that when inversion symmetry is broken, at a transition between different \mathbb{Z}_2 topological numbers [35, 36], i.e. between a strong topological insulator (STI) and a normal insulator (or a weak topological insulator (WTI)), a Weyl semimetal (WSM) phase always appears, as is expected from Ref. [1]. This theory can be applied to any inversion asymmetric crystals, such as BiTeI under high pressure [6] and Te under pressure [34].

Setup of the problem— We consider a Hamiltonian matrix $H(\mathbf{k}, m)$ where \mathbf{k} is a Bloch wavevector, and m is an external parameter controlling the gap. Furthermore, we assume that a space group of the system remains the same for any values of m . To see how the gap closes, we assume that for $m < m_0$ the system is an insulator, and that at $m = m_0$ the gap closes at a wavevector $\mathbf{k} = \mathbf{k}_0$. We assume the Hamiltonian to be analytic with respect to \mathbf{k} and m . We then expand the Hamiltonian in terms of $m - m_0$ and $\mathbf{q} \equiv \mathbf{k} - \mathbf{k}_0$, and retain some terms of lower order, in order to see evolution of the band structure for $m > m_0$. We consider all the 138 space groups without inversion symmetry, for the purpose of application to real materials. For each space group, there are various \mathbf{k} points such as Γ , X and L . Each \mathbf{k} point is associated with a k -group (little group), which leaves the \mathbf{k} point unchanged. In order to focus on the closing of the gap, we retain only the lowest conduction band and the highest valence band, whose irreducible representations (irreps) of the k -group at \mathbf{k}_0 are denoted as R_v and

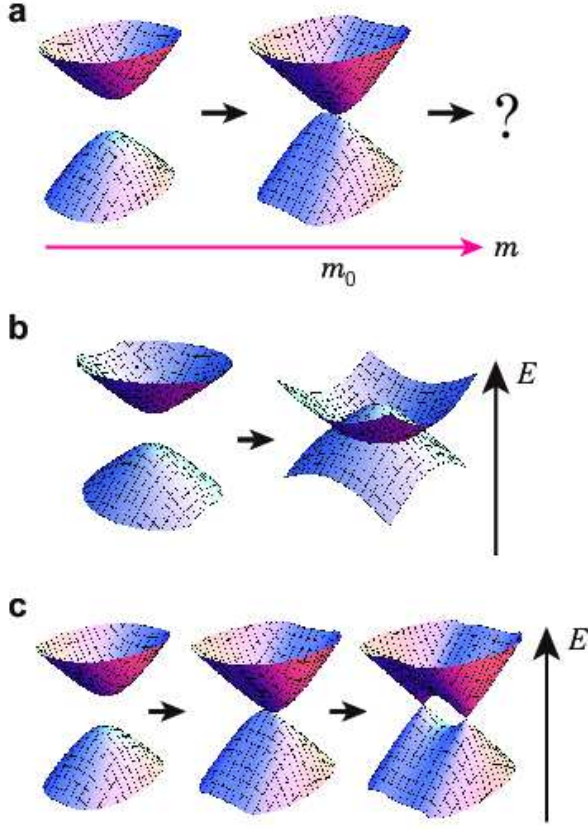


FIG. 1. Setup of our main problem of band evolution in an inversion-symmetric semiconductor. **a**: Band evolution towards gap closing. Schematic illustrations for two classes of band evolution into **b**: a nodal-line semimetal, i.e. semimetal with a gap closing along a loop, and **c**: a Weyl semimetals

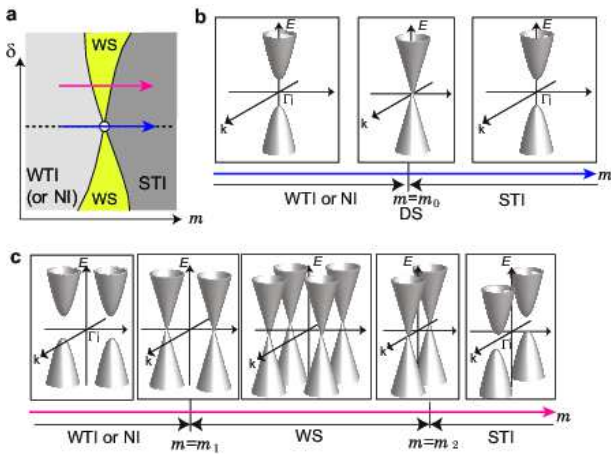


FIG. 2. **a**, Universal phase diagram for Z_2 topological phase transitions. It is shown as a function of an external parameter m and a parameter δ controlling a degree of inversion symmetry breaking [1]. The horizontal dotted line is the inversion-symmetry line. **b**, **c**, Evolutions of bulk band structure with a change of the parameter m , for inversion-symmetric (**b**) and inversion-asymmetric (**c**) cases, respectively. The blue and the red arrows in **a** corresponds to the cases **b** and **c**, respectively.

R_c , respectively. In our analysis, we use the complete list of double-valued irreps of k -groups in Ref. [37].

Varieties of 138 space groups, \mathbf{k} points for each space group, and irreps at each \mathbf{k} point lead to numerous possibilities. Our theory in this paper exhausts all the cases; in fact, we can substantially reduce the number of possible cases by the following considerations. First, we can exclude cases with $\dim R_v \geq 2$ or $\dim R_c \geq 2$, i.e. the cases where the valence or the conduction band at \mathbf{k}_0 have degeneracy; it is because the gap does not close at \mathbf{k}_0 . The reason is the following. If $\dim R_c \geq 2$ at \mathbf{k}_0 , the energy of the conduction band does not have a minimum at this \mathbf{k}_0 point, because the degenerate states at \mathbf{k}_0 will split linearly away from \mathbf{k}_0 along a generic direction (see Fig. 3a). Therefore the gap does not close at \mathbf{k}_0 . A similar argument applies to the valence band. Thus we can safely restrict ourselves to the cases with $\dim R_v = \dim R_c = 1$; hence, the effective model is described by a 2×2 Hamiltonian matrix, which drastically simplifies our analysis. In particular, among possible wavevectors \mathbf{k}_0 , we exclude the time-reversal invariant momenta (TRIM), because the bands at the TRIM always have Kramers degeneracies.

Various cases of gap-closing events classified by symmetry— Next, we determine the Hamiltonian matrix $H(\mathbf{k}, m)$ for each case from R_v and R_c . Resulting behaviors of the closing of the gap are then classified in term of R_v and R_c . All the cases for 138 space groups are summarized in the tables in the Supplemental Material. Here, we briefly explain some representative cases of k -groups, and their details are given in the Methods section. In the analysis here, in addition to point-group elements of a k -group, we have to consider symmetry operations of a form ΘO , where Θ is a time-reversal operation and O is a point-group element.

(i) no symmetry: We consider a generic \mathbf{k} point having no special symmetry; namely, a k -group consists only of an identity operation. The band gap can close there, and the closing of the gap always accompanies a pair creation of Weyl nodes, as shown in Ref. [1, 38]. This occurs because Weyl nodes are topological, having quantized monopole charges $q = \pm 1$ for the \mathbf{k} -space Berry curvature; this topological property allows pair creation of Weyl nodes with $q = +1$ and $q = -1$. We call this case of Weyl-node creation as “1”, where 1 represents a number of monopole-antimonopole pairs (Fig. 3b).

(ii) C_2 symmetry: Suppose the \mathbf{k} -group consists only of the twofold (C_2) symmetry. Then there are two one-dimensional (1D) irreps with opposite signs of the C_2 eigenvalues. Consequently we have two cases: (ii-1) $R_c = R_v$ and (ii-2) $R_c \neq R_v$. For (ii-1): $R_c = R_v$, the gap cannot close by changing m , because of level repulsion. On the other hand, for (ii-2): $R_c \neq R_v$, the gap can close because there is no level repulsion at \mathbf{k}_0 , and we find that the closing of the gap accompanies creation of a pair of Weyl nodes. When m is increased, the two Weyl nodes (a monopole and an antimonopole) move along the C_2 axis, as shown in Fig. 3c. We call this case “1a”, where 1 represents the number of monopole-antimonopole pairs, and a means “axial”, i.e. the relative direction between the two

Weyl nodes is along a high-symmetry axis.

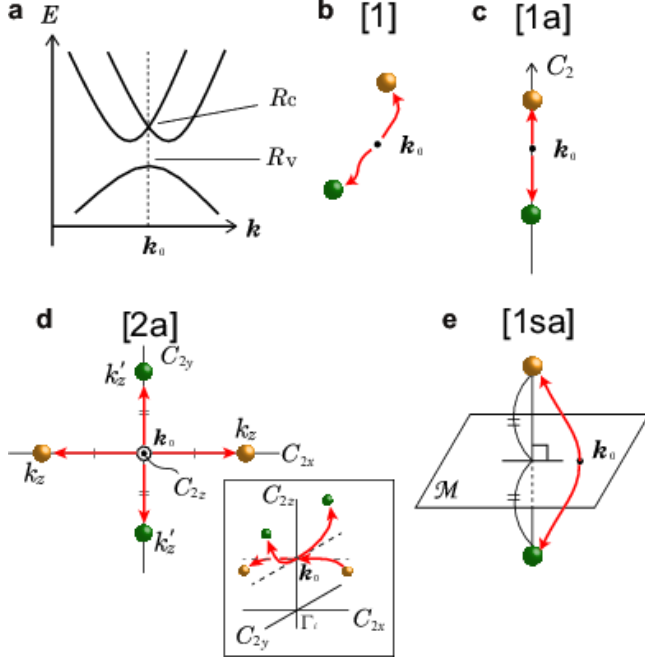


FIG. 3. **a**, Schematic band structure for the case with $\dim R_c = 2$ and $\dim R_v = 1$. The gap does not close at \mathbf{k}_0 in this case. **b**, Trajectory of Weyl nodes in (i) after pair creation at \mathbf{k}_0 . **c**, Trajectory of Weyl nodes in (ii-2) and in (iii-2). The Weyl nodes move along the C_2 axis. **d**, Trajectory of Weyl nodes in the case (iii-1), viewed from different angles. The \mathbf{k}_0 point is on the C_{2z} axis away from a TRIM Γ_i . **e**, Trajectory of Weyl nodes in the case (iv-1). In **b-e**, yellow and green spheres denote monopoles and antimonopoles in \mathbf{k} space, respectively, and they are both Weyl nodes.

(iii) C_2 and ΘC_2 symmetries: The problem becomes more complicated when the time-reversal operator Θ is involved. Here, we consider a system with two C_2 symmetries C_{2y} , C_{2z} , whose rotational axes (y and z) cross perpendicularly. We focus on a \mathbf{k}_0 point lying on the C_{2z} axis, but not on the C_{2y} axis; the k -group then consists of C_{2z} and ΘC_{2y} . There are two eigenvalues of C_{2z} with opposite signs, yielding two irreps, and R_c and R_v can take either of these two irreps. We consider two cases (iii-1) $R_c = R_v$, and (iii-2) $R_c \neq R_v$ separately. For (iii-1) $R_c = R_v$, the closing of the gap leads to creations of two monopoles and two antimonopoles, and their trajectories are shown in Fig. 3d. As compared to (ii-1), the additional ΘC_{2y} symmetry suppresses level repulsion at \mathbf{k}_0 , and therefore the gap can close. In our list this behavior is called **2a**. Here **2** means the number of monopole-antimonopole pairs, and **a** means that the relative orientation between the two monopoles (and likewise the two antimonopoles) is fixed to be along high-symmetry axes. For (iii-2) $R_c \neq R_v$, a pair of Weyl nodes are created and they move along the C_{2z} axis as in (ii-2) (Fig. 3c). It is written as **1a**.

(iv) mirror symmetry \mathcal{M} : We consider the k -group consisting only of a mirror symmetry or a glide symmetry. There are two representations with opposite signs of mirror (or glide)

eigenvalues. In the case (iv-1): $R_c = R_v$, the gap can close, leading to a creation of a pair of Weyl nodes. The trajectory of the monopole and that of the antimonopole are mirror images to each other. We call this pattern **1sa**, representing that the direction between the two Weyl nodes are always perpendicular to the mirror plane (Fig. 3e). The symbol **s** means that all the Weyl nodes are related by symmetry operations, and therefore they are at the same energy. On the other hand, for (iv-2): $R_c \neq R_v$, the gap closes along a loop (i.e. nodal line) within the mirror plane in \mathbf{k} space. We call this case **1l**, where **l** stands for “loop” and **1** represents the number of loops. This degeneracy along the loop occurs because on the mirror plane there is no level repulsion between the valence and the conduction bands, belonging to the different irreps.

138 inversion-asymmetric space groups— We can similarly calculate band-structure evolution after closing of the gap for all the high-symmetry points and lines for the 138 space groups without inversion symmetry. A complete list of all the cases is lengthy and is summarized in the tables in the Supplemental Material. In Fig. 4, we summarize possible patterns for positions where the gap closes in \mathbf{k} space for $m > m_0$, i.e. after closing of the gap at \mathbf{k}_0 . In the figure, the individual patterns are represented as **1sp**, **1l**, and so on, and their notations are explained in the caption.

From this analysis, we conclude that there are only two possibilities after closing of the gap in inversion-asymmetric insulators with time-reversal symmetry: nodal-line semimetals and Weyl semimetals. The nodal-line semimetals are denoted as $n\ell$ ($n = 1, 2, 3, 4, 6$) (See Fig. 4a). Here n is the number of nodal-lines on mirror planes, on which the highest valence and the lowest conduction bands have different mirror eigenvalues. The other possibility is the Weyl semimetal, shown in Fig. 4b-q. In some \mathbf{k} with high symmetry, Weyl nodes and nodal lines are simultaneously generated. Remarkably, an ITI transition never occurs in closing of the gap of the inversion-asymmetric insulators.

Materials realization— This universal result applies to any crystalline materials without inversion symmetry, as we show some examples in the following. Our first example is tellurium (Te), which has been theoretically shown to become a WSM at high pressure [7]. Tellurium is a narrow gap semiconductor without inversion symmetry, with its space group No.152 ($P3_121$) or No.154 ($P3_221$), which are mirror images to each other. At higher pressure, the gap closes and eventually a pair of Weyl nodes is produced at each of the four P points on the K-H lines. The Weyl nodes then move along the C_3 axes (K-H lines). According to our table, the only possibility of the gap closing is **1a**, in agreement with the above result. Moreover, this **1a** at the P points is allowed only when the C_3 eigenvalues of the valence and conduction bands are different; it was confirmed by the *ab initio* calculation [7].

The second example is $\text{HgTe}_x\text{S}_{1-x}$ under strain, which has been shown to become a WSM [10]. It has zinc-blende structure (space group No.216, $F\bar{4}3m$), but a strain along the [001] direction reduces the space group to No.119 ($I\bar{4}m2$). In this case, when x is increased from $x = 0$, the gap closes at four

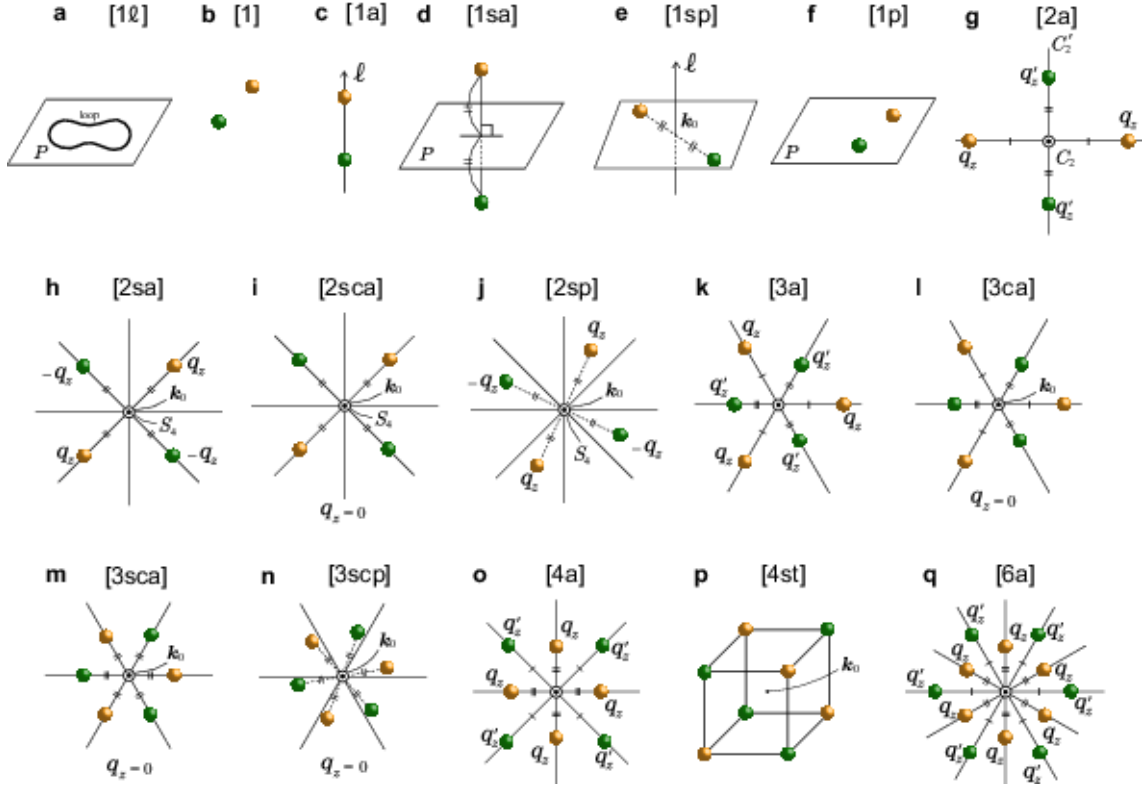


FIG. 4. All the patterns of locations of gap-closing points after parametric gap closing. **a**, A line node for a nodal-line semimetal. While the figure shows the case with a single line node, the number of line nodes can range among 1, 2, 3, 4 and 6. **b-p**, All the patterns of Weyl nodes after parametric gap closing at \mathbf{k}_0 . Yellow and green spheres denote monopoles and antimonopoles in \mathbf{k} space, and they are both Weyl nodes. Solid lines denote high-symmetry directions. In **g-o** and **q**, The z axis, taken to be perpendicular to the page, is parallel to a high-symmetry axis. $\mathbf{q} \equiv \mathbf{k} - \mathbf{k}_0$ is the momentum measured from \mathbf{k}_0 . In **i**, **l**, **m** and **n**, all the Weyl nodes are coplanar with \mathbf{k}_0 , while in **g**, **h**, **j**, **k**, **o**, and **q**, the Weyl nodes are mutually displaced along the z direction. The numbers in the figures **b-q** represent the number of pairs of Weyl nodes, except for **1 ℓ** , **2 ℓ** , **3 ℓ** , **4 ℓ** , and **6 ℓ** , where the number represents the number of loops. The symbol ℓ means that there are nodal lines where the gap is closed. Such nodal lines always appear on mirror planes, and only when the valence and the conduction bands have different mirror eigenvalues. The symbol **a** (axial) represents that the relative directions between the Weyl nodes are fixed to be along certain high-symmetry lines; meanwhile, the symbol **p** (planar) represents that such directions are not confined along high-symmetry axes, but confined within high-symmetry planes. The symbol **c** (coplanar) means that all the monopoles and antimonopoles lie on a same high-symmetry plane. This symbol **c** is used only when there are more than one monopole-antimonopole pairs. The symbol **t** (tetrahedron) appears only for a few cases with tetrahedral or cubic symmetries. It means that 4 monopoles and 4 antimonopoles form 8 vertices of a cube whose center is a high symmetry point, and 4 monopoles form a tetrahedron. The symbol **s** (symmetric) means that all the monopoles and the antimonopoles are related to each other by symmetry operations. In such cases they are energetically degenerate, and it is possible to locate all the Weyl nodes on the Fermi energy. Otherwise, these monopoles and antimonopoles may not necessarily be at the same energy.

points on the Γ -K lines (Σ points) on the (110) and the (1 $\bar{1}$ 0) mirror planes, and four pairs of Weyl nodes are created. The eight Weyl points then move within the $k_z = 0$ plane by a further increase of x , until they mutually annihilate at Σ points after $\pm\pi/2$ rotation around the [001] axis [10]. According to our table, the gap closing at each Σ point corresponds to **1sa**, meaning that the Weyl nodes move perpendicular to the (110) or the (1 $\bar{1}$ 0) mirror planes. It agrees with the previous work [10].

Because degeneracies in topological semimetals are accidental, efficient and systematic search of topological semimetals is difficult. Moreover, such degeneracies occur at generic \mathbf{k} points; therefore, they may easily be overlooked in *ab initio* calculations, where band structure is usually calculated

only along high-symmetry lines. Thus, a search of topological semimetals has been an elusive issue.

Our results can be used for search of topological semimetal materials. For example, we find that HfS has nodal lines near the Fermi level. HfS has a valley of the density of states near the Fermi level because of the following two reasons. One is covalent bonds from S $3p$ orbitals, by which valence electrons in p orbitals tend to make a gap at the Fermi level to lower the total energy; it is prominent for atoms with large electronegativity. The other is an open shell of Hf $5d$ orbital ($5d^2$) having strong SOC. The structure of HfS is the same as that of tungsten carbide (WC) (Fig. 5 **a**), with the space group No.187 ($P6m2$) [39]. Figure 5 **b** shows electronic band structure of HfS. If the SOC is neglected, Dirac nodal lines exist

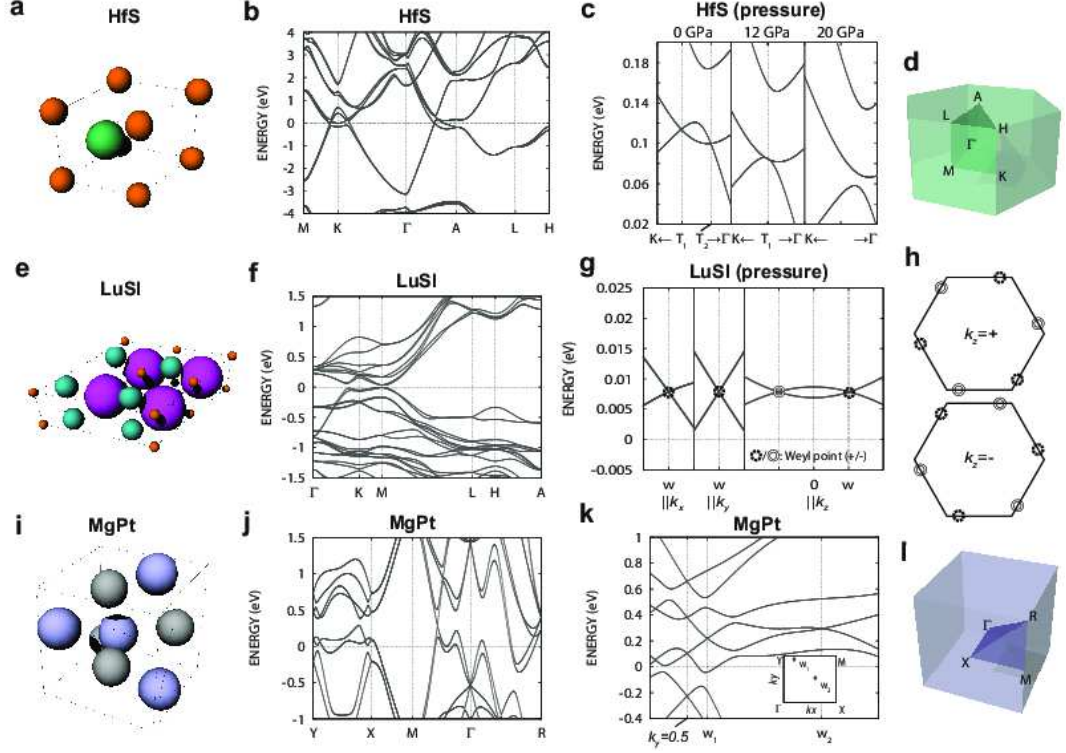


FIG. 5. **a**, Crystal structure of HfS. **b**, **c**, electronic band structure of HfS. **c** shows the phase transition of HfS under pressure. T_1 and T_2 are the points of the intersection of the nodal-line with $K\Gamma$ line. **d**, Brillouin zone of HfS. **e**, Crystal structure of LuSI. **f**, **g**, Electronic band structure of LuSI. **g** Band structure of LuSI under pressure, where lattice constant c is multiplied by 0.945. **h** Positions of the Weyl nodes of LuSI under pressure on the $k_z = 0$ plane. **i**, Crystal structure of MgPt. **j**, **k**, electronic band structure of MgPt. **l**, the Brillouin zone of LuSI and MgPt. The energy is measured from the Fermi level.

around the K points on the $k_z = 0$ plane. The SOC lifts the degeneracy of the Dirac nodal lines, and Weyl nodal lines appear instead, near the K points on the mirror plane $k_z = 0$. By applying pressure (Fig. 5 **c**) or by atomic substitution from S to Se, the nodal lines become smaller. At 9 GPa, the nodal lines shrink to points (T points) on the $K\Gamma$ lines, and then the gap opens above 9 GPa. This evolution of the band structure corresponds to **1f** in our table.

Next, we show LuSI as a Weyl semimetal under pressure. The conduction and the valence bands originate from Lu $6s + 5d$ orbitals, and S $3p$ (and I $5p$) orbitals, respectively. The structure type of LuSI is GdSI (Fig. 5 **e**), with the space group No.174 ($P\bar{6}$) [40]. Each type of atoms constitutes a distorted trigonal lattice, which displaces the gap away from the Γ point. Figure 5 **f** shows electronic structure of LuSI, having a very narrow gap (< 0.04 eV) near the M point. It becomes a Weyl semimetal under pressure, as shown in Fig. 5 **g** [41]. There exist 6 monopoles and 6 antimonopoles at the same energy because they are related by symmetry. By applying pressure, the band gap first closes at six generic points on the $k_z = 0$ plane, related with each other by sixfold symmetry. It corresponds to **1sa** because of the mirror symmetry M_z , belonging to the case (iv-1).

We show another example, MgPt, as a material having Weyl nodes. MgPt has the FeSi-type structure (Fig. 5 **i**) having the

space group No.198 ($P2_13$) [42]. Figures 5 **j**, **k** show electronic structure of MgPt. The band near the Fermi level originates from Pt $5d$ orbitals having strong SOC. Weyl nodes w_1 and w_2 exist at general \mathbf{k} points with no symmetry.

Topological phase transitions and Z_2 topological number— Let us turn to Z_2 phase transitions in three dimensions, i.e. STI-NI (or STI-WTI) phase transitions. In the universal phase diagram (Fig. 2 **a**) between a STI and a NI (or a WTI), there should be a finite region of a Weyl semimetal phase when inversion symmetry is broken as shown in the previous works [1, 38]; nevertheless in its derivation [1], crystallographic symmetries except for inversion symmetry are not considered. The result in the present paper shows that this conclusion of existence of the Weyl semimetal phase in the Z_2 phase transition holds true in general, whenever inversion symmetry is broken. One of the remarkable conclusions here is that an ITI transition never occurs in inversion-asymmetric crystals. This is in strong contrast with inversion-symmetric systems, where a transition between different Z_2 topological phases always occurs as an ITI transition (i.e. at a single value of m), as seen in $\text{TlBi}(\text{S}_{1-x}\text{Se}_x)_2$ at around $x \sim 0.5$ [43, 44].

We apply this theory to BiTeI, which lacks inversion symmetry [45]. The space group of BiTeI is No.156 ($P3m1$). BiTeI is a NI at ambient pressure, and has been proposed to become a STI at high pressure [46, 47]. Subsequently, *ab ini-*

tio calculations in a previous work [6] showed existence of a Weyl semimetal phase between the NI and the STI phases in a narrow window of pressure, which had been overlooked in some previous works [46, 47]. When the pressure is increased, the gap first closes at six S points on the A-H lines, and six pairs of Weyl nodes are created. The six monopoles and six antimonopoles move in opposite directions; subsequently, they annihilate each other at generic points on three mirror planes, leading to the STI phase [6]. Combination of all the trajectories of the Weyl nodes yields a loop around the TRIM point (A point); it means that a band inversion occurs at the A point between the low-pressure NI phase and the high-pressure STI phase, and subsequent change of the \mathbb{Z}_2 topological number results [1, 38]. From our table, the space group No.156 at six S points gives **1sp**, meaning that immediately after the pair creations, they move perpendicular to the AH line, in agreement with the previous work [6].

Other examples are $\text{LaBi}_{1-x}\text{Sb}_x\text{Te}_3$ and $\text{LuBi}_{1-x}\text{Sb}_x\text{Te}_3$, which has been proposed to undergo NI-WSM-TI phase transition by changing x [6]. The space group is No.160 ($R3m$), lacking inversion symmetry. By increasing x the band gap closes at six generic points, corresponding to creation of Weyl nodes [6]. The resulting 12 Weyl nodes move in \mathbf{k} space, until they are annihilated at the six $B(\equiv \Sigma)$ points. In our table, the B point corresponds to **1sp**, i.e. the pair annihilation occurs between two Weyl nodes, which are moving perpendicular to the normal direction of the mirror planes. It agrees with the previous work 6.

Summary– To summarize, we investigate evolution of the band structure after parametric closing of the band gap in inversion-asymmetric crystals. We found that there occur only two possibilities. One is the Weyl semimetal phase, and closing of the gap corresponds to monopole-antimonopole pair creations of Weyl nodes. Distribution of the Weyl nodes in \mathbf{k} space after the closing of the gap is uniquely determined by symmetry. The other possibility is a nodal-line semimetal, with a gap closed along loops on mirror planes. From these results, we show that in any topological phase transitions with different \mathbb{Z}_2 topological numbers (without inversion symmetry), there should be a Weyl semimetal phase between the two bulk-insulating phases. These results give us a systematic way to search materials for topological semimetals.

Methods

Details of the first-principles calculation– Electronic structure is obtained from the local density approximation (LDA) of the relativistic density functional theory (DFT). Calculation of the electronic structure is carried out using OpenMX code (<http://www.openmx-square.org/>) based on localized basis functions and norm-conserving pseudopotentials. We employ $12 \times 12 \times 12$ \mathbf{k} -point sampling for HfS, HfSe, and MgPt, and $6 \times 6 \times 12$ \mathbf{k} -point sampling for LuSI. Lattice optimization for HfS under pressure is based on the LDA, and is carried out using QMAS (Quantum MAterials Simulator) code (<http://qmas.jp/>) based on the projector augmented-wave method. We employ $12 \times 12 \times 12$ \mathbf{k} -point sampling and 40 Ry as a plane-wave energy cutoff in the lattice optimization.

Details of the effective-model calculation

It is convenient in the following analysis to expand the Hamiltonian as $H(\mathbf{q}, m) = \sum_{i=1}^3 a_i(\mathbf{q}, m)\sigma_i$, where σ_i ($i = x, y, z$) are Pauli matrices,

$\mathbf{q} = \mathbf{k} - \mathbf{k}_0$. and $\sigma_z = +1$ and -1 correspond to the conduction and the valence band, respectively. Here we omitted the term proportional to an identity matrix because it does not affect the gap-closing event. Since the gap closes at $m = m_0$, $\mathbf{q} = 0$, we have $a_i(\mathbf{q} = 0, m = m_0) = 0$, $i = 1, 2, 3$. We assume that when $m < m_0$ the gap is open. In each case presented below, we examine whether the gap can close or not by counting a codimension d_c , i.e. the number of parameters to be tuned to close the gap. If the codimension is equal or lower than the number of tunable variables, the gap can close there; otherwise the gap does not close.

(i) **no symmetry**: When there is no special symmetry at the \mathbf{k} point, the Hamiltonian is not restricted by symmetry. The gap of the 2×2 Hamiltonian closes when $a_x = a_y = a_z = 0$; this condition determines a curve in the four-dimensional space (\mathbf{q}, m) . This curve goes through the point $(\mathbf{q} = 0, m = m_0)$, but it does not exist in the $m < m_0$ region by assumption, and therefore the curve has a minimum value of m at $m = m_0$ (Fig. 6 a). Therefore, as the value of m increases, the gap-closing point appears at $\mathbf{q} = 0$ for $m = m_0$ and then it splits into two points (Weyl nodes) when m is increased further. It is a pair creation of a monopole and an antimonopole.

(ii) **C_2 symmetry**: Suppose \mathbf{k} is invariant only by a twofold (C_2) rotation, taken to be around the z axis. For (ii-1): $R_c = R_v$, the 2×2 Hamiltonian satisfies $H(q_x, q_y, q_z, m) = H(-q_x, -q_y, q_z, m)$, where $\mathbf{q} \equiv \mathbf{k} - \mathbf{k}_0$. In particular, at $\mathbf{k} = \mathbf{k}_0$, the above equation becomes trivial, imposing no constraint on the Hamiltonian. Therefore, the gap cannot close by changing a single parameter m , because three conditions $a_i(\mathbf{q} = 0, m) = 0$, ($i = x, y, z$) cannot be simultaneously satisfied in general.

On the other hand, for (ii-2): $R_c \neq R_v$, the opposite signs of the C_2 eigenvalues lead to an equation $H(q_x, q_y, q_z, m) = \sigma_z H(-q_x, -q_y, q_z, m) \sigma_z$. In particular, for $q_x = q_y = 0$, we obtain $H(0, 0, q_z, m) = a_z(q_z, m)\sigma_z$, whose gap closes when $a_z(q_z, m) = 0$. From our assumption, it is satisfied when $q_z = 0, m = m_0$ but is not for $m < m_0$. Hence, the value of m satisfying $a_z(q_z, m) = 0$ as a function of q_z should have a minimum at $q_z = 0$ (Fig. 6 b). It leads to bifurcation into two solutions on the q_z axis, as m increases across m_0 , and it describes a monopole-antimonopole pair creation of Weyl nodes. Therefore two Weyl nodes are created at $m = m_0$, and they move along the C_2 axis. We call this case as “1a”.

(iii) **C_2 and ΘC_2 symmetries**: Suppose the wavevector \mathbf{k} is invariant under C_{2z} and ΘC_{2y} . There are two eigenvalues of C_{2z} with opposite signs, yielding two irreps. For (iii-1) $R_c = R_v$, the Hamiltonian satisfies $H(q_x, q_y, q_z, m) = H(-q_x, -q_y, q_z, m) = H^*(q_x, -q_y, q_z, m)$, where $*$ represents complex conjugation. These equations lead to $a_x = f_x(q_x^2, q_y^2, q_z, m)$, $a_y = q_x q_y f_y(q_x^2, q_y^2, q_z, m)$, $a_z = f_z(q_x^2, q_y^2, q_z, m)$. As m is increased, it describes creations of two monopoles and two antimonopoles at $\mathbf{q} = 0, m = m_0$. For $m > m_0$, two monopoles are at $(\pm \tilde{q}_x, 0, \tilde{q}_z)$ on the xz plane and two antimonopoles are at $(0, \pm \tilde{q}_y, \tilde{q}_z')$, where $\tilde{q}_x, \tilde{q}_y, \tilde{q}_z$ and \tilde{q}_z' depend on m (or the positions of the monopoles and antimonopoles might be exchanged). Notably, in contrast to (ii-1) where the level repulsion prohibits closing of the gap, in the present case (iii-1), the additional ΘC_2 symmetry gives rise to additional constraints and suppresses level repulsion. In our list this behavior in (iii-1) is represented as **2a**.

For (iii-2) $R_c \neq R_v$, the Hamiltonian satisfies $H(q_x, q_y, q_z, m) = \sigma_z H(-q_x, -q_y, q_z, m) \sigma_z = H^*(q_x, -q_y, q_z, m)$. The similar discussion as in (iii-1) leads to the result $a_x = q_x f_x(q_x^2, q_y^2, q_z, m)$, $a_y = q_y f_y(q_x^2, q_y^2, q_z, m)$, $a_z = f_z(q_x^2, q_y^2, q_z, m)$. Therefore, for $q_x = q_y = 0$, a_x and a_y identically vanish, and the remaining condition $a_z(0, 0, q_z, m) = 0$ describes a pair creation of Weyl nodes at $\mathbf{q} = 0$ and $m = m_0$ as in (ii-2). It is written as **1a**.

(iv) **mirror symmetry \mathcal{M}** : let the z axis denote the direction normal to the mirror plane. Because a square of the mirror operation

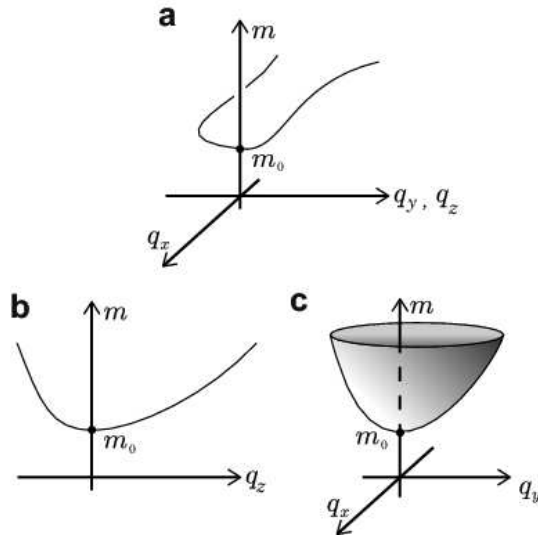


FIG. 6. Values of m for closing of the gap as a function of \mathbf{q} . **a** $m = m(q_x, q_y, q_z)$ as a solution of $a_i(q_x, q_y, q_z, m) = 0$ ($i = x, y, z$) in (i). **b**, $m = m(q_z)$ that satisfies $a_z(0, 0, q_z, m) = 0$ in (ii-2). **c**: $m = m(q_x, q_y)$ as a solution of $a_z(q_x, q_y, 0, m) = 0$ in (iv-2).

M is equal to -1 for mirror symmetry or an identity operation times a \mathbf{k} -dependent factor for glide symmetry, there are two representations with opposite signs of mirror eigenvalues. For (iv-1): $R_c = R_y$, the Hamiltonian satisfies $H(q_x, q_y, q_z, m) = H(q_x, q_y, -q_z, m)$. This equation is automatically satisfied on the mirror plane $q_z = 0$. Thus closing of the gap on the mirror plane imposes three conditions $a_i(q_x, q_y, 0, m) = 0$, $i = x, y, z$ for three variables q_x , q_y , and m . This set of equations can have solutions on the mirror plane, and this closing of the gap accompanies a pair creation of Weyl nodes, which will then move symmetrically with respect to the mirror plane. We call this pattern **1sa**.

On the other hand, for (iv-2): $R_c \neq R_y$, we obtain $H(q_x, q_y, q_z, m) = \sigma_z H(q_x, q_y, -q_z, m) \sigma_z$. Hence, within the $q_z = 0$ plane, the Hamiltonian is expressed as $H(q_x, q_z, 0, m) = a_z(q_x, q_y, 0, m) \sigma_z$. Closing of the gap imposes only one condition $a_z = 0$ (i.e. $d_c = 1$) for three variables (q_x, q_y, m) ; therefore, the gap can close by changing m . By assumption, the gap-closing condition, $a_z(q_x, q_y, 0, m) = 0$, does not have solutions for $m < m_0$ and have a solution at $q_x = q_y = 0, m = m_0$. Therefore, the value of m as a function of q_x and q_y has a minimum at $q_x = q_y = 0$ as shown in Fig. 6c. When m is larger than m_0 , the gap closes along a loop (nodal line) within the $q_z = 0$ plane. We call this case **1f**.

[1] Murakami, S. Phase transition between the quantum spin hall and insulator phases in 3D: emergence of a topological gapless phase. *New J. Phys.* **9**, 356 (2007).
 [2] Wan, X., Turner, A. M., Vishwanath, A. & Savrasov, S. Y. Topological semimetal and Fermi-arc surface states in the electronic structure of pyrochlore iridates. *Phys. Rev. B* **83**, 205101 (2011).
 [3] Wang, Z. *et al.* Dirac semimetal and topological phase transitions in $A_3\text{Bi}$ ($A = \text{Na, K, Rb}$). *Phys. Rev. B* **85**, 195320 (2012).
 [4] Wang, Z., Weng, H., Wu, Q., Dai, X. & Fang, Z. Three-dimensional Dirac semimetal and quantum transport in Cd_3As_2 . *Phys. Rev. B* **88**, 125427 (2013).

[5] Xu, G., Weng, H., Wang, Z., Dai, X. & Fang, Z. Chern Semimetal and the Quantized Anomalous Hall Effect in HgCr_2Se_4 . *Phys. Rev. Lett.* **107**, 186806 (2011).
 [6] Liu, J. & Vanderbilt, D. Weyl semimetals from noncentrosymmetric topological insulators. *Phys. Rev. B* **90**, 155316 (2014).
 [7] Hirayama, M., Okugawa, R., Ishibashi, S., Murakami, S. & T. Miyake. Weyl Node and Spin Texture in Trigonal Tellurium. *Phys. Rev. Lett.* **114**, 206401 (2015).
 [8] Weng, H., Fang, C., Fang, Z., Bernevig, B. A. & Dai, X. Weyl semimetal phase in noncentrosymmetric transition-metal monophosphides. *Phys. Rev. X* **5**, 011029 (2015).
 [9] Huang, S.-M. *et al.* A Weyl fermion semimetal with surface Fermi arcs in the transition metal monpnictide TaAs class. *Nat. Commun.* **6**, 7373 (2015).
 [10] Rauch, T., Achilles, S., Henk, J. & Mertig, I. Spin Chirality Tuning and Topological Semimetals in Strained $\text{HgTe}_{x}\text{S}_{1-x}$. *Phys. Rev. Lett.* **114**, 236805 (2015).
 [11] Huang, S.-M., Xu, S.-Y., Belopolski, I., Lee, C.-C., Chang, G., Wang, B., Alidoust, N., Neupane, M., Zheng, H., Sanchez, D., Bansil, A., Bian, G., Lin, H. & Hasan, M. Z. A new type of Weyl semimetal with quadratic double Weyl fermions in SrSi_2 . arXiv:1503.05868
 [12] Soluyanov, A. A., Gresch, D., Wang, Z., Wu, Q., Troyer, M., Dai, X. & Bernevig, B. A. Type-II Weyl semimetals. *Nature* **527**, 495 (2015).
 [13] Xu, S.-Y. *et al.* Discovery of a Weyl fermion semimetal and topological Fermi arcs. *Science* **349**, 613–617 (2015).
 [14] Lv, B. Q. *et al.* Experimental discovery of Weyl semimetal TaAs. *Phys. Rev. X* **5**, 031013 (2015).
 [15] Lv, B. *et al.* Observation of Weyl nodes in TaAs. *Nat. Phys.* **11**, 724–727 (2015).
 [16] Berry M. V. *Proc. Roy. Soc. London Ser A* **392**, 45 (1984)
 [17] Volovik, G. E. *The universe in a helium droplet* (Oxford University Press, 2009).
 [18] Ojanen, T. Helical Fermi arcs and surface states in time-reversal invariant Weyl semimetals. *Phys. Rev. B* **87**, 245112 (2013).
 [19] Okugawa, R. & Murakami, S. Dispersion of Fermi arcs in Weyl semimetals and their evolutions to Dirac cones. *Phys. Rev. B* **89**, 235315 (2014).
 [20] Haldane, F. D. M. Attachment of Surface "Fermi Arcs" to the Bulk Fermi Surface: "Fermi-Level Plumbing" in Topological Metals. arXiv:1401.0529.
 [21] Zyuzin, A. A. & Burkov, A. A. Topological response in Weyl semimetals and the chiral anomaly. *Phys. Rev. B* **86**, 115133 (2012).
 [22] Burkov, A. A., Hook, M. D. & Balents L. Topological nodal semimetals. *Phys. Rev. B* **84**, 235126 (2011).
 [23] Mullen, K., Uchoa, B. & Glatzhofer, D. T. Line of dirac nodes in hyperhoneycomb lattices. *Phys. Rev. Lett.* **115**, 026403 (2015).
 [24] Fang, C., Chen, Y., Kee, H.-Y. & Fu, L. Topological nodal line semimetals with and without spin-orbital coupling. *Phys. Rev. B* **92**, 081201 (2015).
 [25] Chen, Y. *et al.* Nanostructured carbon allotropes with Weyl-like loops and points. *Nano Lett.* **15**, 6974–6978 (2015).
 [26] Weng, H. *et al.* Topological node-line semimetal in three-dimensional graphene networks. *Phys. Rev. B* **92**, 045108 (2015).
 [27] Kim, Y., Wieder, B. J., Kane, C. L. & Rappe, A. M. Dirac line nodes in inversion-symmetric crystals. *Phys. Rev. Lett.* **115**, 036806 (2015).
 [28] Yu, R., Weng, H., Fang, Z., Dai, X. & Hu, X. Topological node-line semimetal and Dirac semimetal state in antiperovskite Cu_3PdN . *Phys. Rev. Lett.* **115**, 036807 (2015).
 [29] Xie, L. S. *et al.* A new form of Ca_3P_2 with a ring of Dirac nodes. *APL Mat.* **3** (2015).

- [30] Chan, Y.-H., Chiu, C.-K., Chou, M. & Schnyder, A. P. Ca_3P_2 and other topological semimetals with line nodes and drumhead surface states. *Phys. Rev. B* **93**, 205132 (2016).
- [31] Zeng, M. *et al.* Topological semimetals and topological insulators in rare earth mononpnictides. Preprint at <http://arxiv.org/abs/1504.03492> (2015).
- [32] Yamakage, A., Yamakawa, Y., Tanaka, Y. & Okamoto, Y. Line-node Dirac semimetal and topological insulating phase in non-centrosymmetric pnictides CaAgX ($X = \text{P, As}$). *J. Phys. Soc. Jpn.* **85**, 013708 (2016).
- [33] Zhao, J., Yu, R., Weng, H. & Fang, Z. Topological node-line semimetal in compressed black phosphorus. Preprint at <http://arxiv.org/abs/1511.05704> (2015).
- [34] Hirayama, M., Okugawa, R., Miyake, T., Murakami, S. Topological Dirac Nodal Lines in fcc Calcium, Strontium, and Ytterbium. Preprint at <http://arxiv.org/abs/1602.06501> (2016).
- [35] Fu, L., Kane, C. L., & Mele, E. J. Topological Insulators in Three Dimensions. *Phys. Rev. Lett.* **98**, 106803.(2007)
- [36] Moore, J. E., & Balents, L., Topological invariants of time-reversal-invariant band structures. *Phys. Rev. B* **75**, 121306 (2007).
- [37] Bradley, C. J., & Cracknell, A. P. *The Mathematical Theory of Symmetry in Solids: Representation Theory for Point Groups and Space Groups* (Oxford Univ Press, Oxford, 2010).
- [38] Murakami, S. & Kuga, S. Universal phase diagrams for the quantum spin Hall systems. *Phys. Rev. B* **78**, 165313 (2008).
- [39] Franzen, H. F. & Graham, J. J. The lower sulphides of hafnium at high temperature. *J. Inorg. Nucl. Chem.* **28**, 377 (1966).
- [40] Dagron C. & Thevet, F. Répartition des types cristallins dans la série des iodosulfures et fluorosulfures des éléments des terres rares et d'yttrium (in French). *C. R. Acad. Sci. Ser. C* **268**, 1867 (1969).
- [41] Because of the extremely small energy gap, numerical error in the structural optimization is larger than the energy scale around the Weyl point at ambient pressure, Therefore, in our calculation, we simply multiply lattice constant c by 0.945 instead of structural optimization. A realistic value of the transition pressure to the Weyl semimetal phase is an open question.
- [42] Stadelmaier H. H. & Hardy W. K. Ternäre Kohlenstofflegierungen von Palladium und Platin mit Magnesium, Aluminium, Zink, Gallium, Germanium, Kadmium, Indium, Zinn, Quecksilber, Thallium und Blei (in German). *Z. Metallkd.* **52**, 391 (1961).
- [43] Xu, S.-Y., Xia, Y., Wray, L. A., Jia, S., Meier, F., Dil, J. H., Osterwalder, J., Slomski, B., Bansil, A., Lin, H., Cava, R. J. & Hasan, M. Z. Topological Phase Transition and Texture Inversion in a Tunable Topological Insulator. *Science* **332**, 560 (2011).
- [44] Sato, T., Segawa, K., Kosaka, K., Souma, S., Nakayama, K., Eto, K., Minami, T., Ando, Y. & Takahashi, T. Unexpected mass acquisition of Dirac fermions at the quantum phase transition of a topological insulator *Nature Phys.* **7**, 840 (2011).
- [45] Ishizaka, K., Bahramy, M. S., Murakawa, H., Sakano, M., Shimojima, T., Sonobe, T., Koizumi, K., Shin, S., Miyahara, H., Kimura, A., Miyamoto, K., Okuda, T., Namatame, H., Taniguchi, M., Arita, R., Nagaosa, N., Kobayashi, K., Murakami, Y., Kumai, R., Kaneko, Y., Onose, Y. & Tokura, Y. Giant Rashba-type spin splitting in bulk BiTeI. *Nature Materials* **10**, 521 (2011).
- [46] Bahramy, M. S., Yang, B.-J., Arita, R. & Nagaosa, N. Emergence of non-centrosymmetric topological insulating phase in BiTeI under pressure. *Nature Communications* **3**, 679 (2012).
- [47] Yang, B.-J., Bahramy, M. S., Arita, R., Isobe, H., Moon, E.-G. & Nagaosa, N. Theory of Topological Quantum Phase Transitions in 3D Noncentrosymmetric Systems. *Phys. Rev. Lett.* **110**

086402 (2013)

Acknowledgement

We thank Shoji Ishibashi for providing us with the *ab initio* code (QMAS) and pseudopotentials. This work is partially supported by JSPS KAKENHI Grant Numbers JP26287062, JP26103006, JP16J08552, and by MEXT Elements Strategy Initiative to Form Core Research Center (TIES).

Additional Information

The authors declare no competing financial interests.

Author contribution

All authors contributed to the main contents of this work. S.M. conceived and supervised the project. S.M. also did analytical calculations for classifications in terms of the space groups with the help of R.O. M.H. performed the *ab initio* calculation with contributions from T.M. R.O. also constructed the theory on real materials such as BiTeI with the help of S.M. M.H., R.O. and S.M. drafted the manuscript. T.M. gave critical revisions of the manuscript.

Supplemental Materials

MORE EXAMPLES FOR GAP CLOSING WITH VARIOUS SYMMETRIES

In the main text we gave four examples for closing of the gap, classified by the \mathbf{k} -group of the \mathbf{k} point considered: (i) no symmetry, (ii) twofold rotation C_2 , (iii) C_2 and $\Theta C'_2$, and (iv) mirror reflection \mathcal{M} . Here we give more examples, in order to demonstrate evolution of the band structure as the value of the parameter m changes. As explained in the Methods section in the main text, we consider the Hamiltonian of the form $H(\mathbf{q}, m) = \sum_{i=1}^3 a_i(\mathbf{q}, m) \sigma_i$, where σ_i ($i = x, y, z$) are Pauli matrices, $\mathbf{q} = \mathbf{k} - \mathbf{k}_0$. We assume $a_i(\mathbf{q} = 0, m = m_0) = 0$, $i = 1, 2, 3$. We also assume that when $m < m_0$ the gap is open.

(v) ΘC_2 symmetry: We consider a \mathbf{k} point which is invariant only under an operation ΘC_2 , where Θ is the time-reversal operation. Let z denote a coordinate along the C_2 axis. The Hamiltonian then satisfies $H(q_x, q_y, q_z, m) = H^*(q_x, q_y, -q_z, m)$. It leads to $a_y = q_z f_y(q_x, q_y, q_z^2, m)$, $a_x = f_x(q_x, q_y, q_z^2, m)$, and $a_z = f_z(q_x, q_y, q_z^2, m)$, where f_i are analytic functions. From these conditions, we can show that the solution at $\mathbf{q} = 0$, $m = m_0$ bifurcates into two Weyl nodes, a monopole and an antimonopole on the $q_z = 0$ plane, and their trajectories are given by $q_z = 0$, $f_x(q_x, q_y, 0, m) = 0 = f_z(q_x, q_y, 0, m)$. This case is denoted as **1p**, where **p** stands for “planar”, meaning that the trajectories of the monopole and the antimonopole are restricted to be within a high-symmetry plane (Fig. S1a).

(vi) $\Theta \mathcal{M}$ symmetry: Suppose the wavevector \mathbf{k} is invariant under $\Theta \mathcal{M}$, where \mathcal{M} is a mirror operation. We take the z axis to be perpendicular to the mirror plane. We then obtain $H(q_x, q_y, q_z, m) = H^*(-q_x, -q_y, q_z, m)$, leading to $a_y = q_x f_x(q_x^2, q_y^2, q_z, m) + q_y f_y(q_x^2, q_y^2, q_z, m)$, while a_x and a_z are analytic functions of q_x^2, q_y^2, q_z and m . By retaining the lowest order in the arguments in these functions, one can see that it describes a monopole-antimonopole pair creation and the positions of the monopole and the antimonopole are expressed as $(\tilde{q}_x(m), \tilde{q}_y(m), \tilde{q}_z(m))$ and $(-\tilde{q}_x(m), -\tilde{q}_y(m), \tilde{q}_z(m))$, respectively. They are symmetric with respect to the $q_x = q_y = 0$ axis. We call this case as **1sp**, where **s** (symmetric) means that the positions of the monopole and the antimonopole are related with each other by symmetry operations (Fig. S1b).

(vii) \mathcal{M} and $\Theta \mathcal{M}'$ symmetries, with mirror planes of \mathcal{M} and \mathcal{M}' perpendicular to each other: Let us call the mirror planes for \mathcal{M} and $\Theta \mathcal{M}'$ as xy and xz planes, respectively. There are two representations corresponding to different signs of the eigenvalues of \mathcal{M} . Evolution of band structure after closing of the gap is different between (vii-1) the two bands with the same irreducible representations ($R_c = R_v$), and (vii-2) those with different irreducible representations ($R_c \neq R_v$). For (vii-1), we have

$$\begin{aligned} H(q_x, q_y, q_z, m) &= H(q_x, q_y, -q_z, m), \\ H(q_x, q_y, q_z, m) &= H^*(-q_x, q_y, -q_z, m), \end{aligned}$$

leading to $a_x = f_x(q_x^2, q_y, q_z^2, m)$, $a_y = q_x f_y(q_x^2, q_y, q_z^2, m)$, $a_z = f_z(q_x^2, q_y, q_z^2, m)$. Therefore, for $q_x = 0$, the gap closes when $f_x(0, q_y, q_z^2, m) = 0 = f_z(0, q_y, q_z^2, m)$ is satisfied. These two equations determine a curve in the (q_y, q_z, m) space, and this curve is symmetric with respect to $q_z \rightarrow -q_z$. This curve passes through the point $q_y = 0, q_z = 0, m = m_0$, but does not go into the $m < m_0$ region. Therefore, as we increase m across m_0 , the solution at $q_y = 0 = q_z, m = m_0$ bifurcates into a pair of Weyl nodes at $\mathbf{q} = (0, \tilde{q}_y(m), \pm \tilde{q}_z(m))$. It is denoted as **1sa** (Fig. S1c). For the case (vii-2) $R_c \neq R_v$, because the mirror symmetry persists for all the \mathbf{k} points within the mirror plane (xy plane), it gives rise to a nodal-line semimetal after closing of the gap, denoted as **1l**.

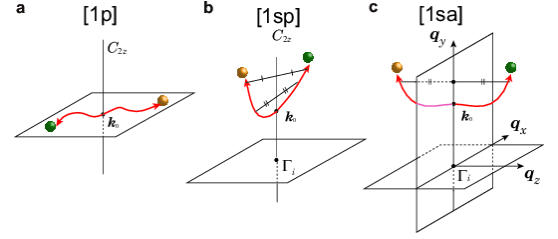


FIG. S1. Trajectories of Weyl nodes after a pair creation at \mathbf{k}_0 for **a**: (v), **b**: (vi), and **c**: (vii-1). Yellow and green spheres denote monopoles and antimonopoles in \mathbf{k} space, respectively, and they are both Weyl nodes.

CLASSIFICATION TABLES FOR EMERGENT TOPOLOGICAL SEMIMETALS AFTER CLOSING OF THE BAND GAP OF INVERSION-ASYMMETRIC INSULATORS

In the main text, we have shown that patterns for emergence of Weyl nodes and nodal lines after closing of the gap are uniquely determined by symmetry, i.e. by the space group and by the value of \mathbf{k}_0 where the gap closes. Here all the patterns for Weyl nodes and nodal lines for all the 138 space groups are shown in Fig. S2. While this figure is the same as Fig. 4 in the main text, and it is shown here again for readers' convenience. Notations used in this figure are summarized as follows.

- The numbers in the symbols in e.g. **1s** and **1sp** represent the number of pair of Weyl nodes, except for **1l**, **2l**, **3l**, **4l**, where the number represents a number of nodal lines.
- The symbol **l** means that there is a nodal line where the gap is closed. Such a nodal line always appears on mirror planes, and only when the valence and the conduction bands have different mirror eigenvalues.
- The symbol **a** (axial) represents that relative directions between the Weyl nodes are fixed to be along certain high-symmetry lines.

- The symbol **p** (planar) represents that relative directions between the Weyl nodes are not confined to be a high-symmetry axis, but confined within a high-symmetry plane.
- The symbol **c** (coplanar) means that all the monopoles and antimonopoles lie on a same high-symmetry plane. This symbol **c** is used only when there are more than one monopole-antimonopole pairs.
- The symbol **t** (tetrahedron) appears only for a few cases with tetrahedral or cubic symmetries. It means that the 4 monopoles and 4 antimonopoles form 8 vertices of a cube whose center is a high symmetry point, and 4 monopoles form a tetrahedron.
- The symbol **s** (symmetric) means that all the monopoles and antimonopoles are related to each other by symmetry operations. In such cases they are energetically degenerate, and it is possible to locate all the Weyl nodes on the Fermi energy. Otherwise, these monopoles and antimonopoles may not necessarily be at the same energy.

Apart from these patterns in Fig. S2, their combinations can appear, such as **1sa1l** (e.g. at K and H points in No.174 and No.187), which means that one pair of Weyl nodes and one nodal-line are simultaneously created at closing of the gap. In addition, when there are more than one mirror planes at \mathbf{k}_0 , more than one nodal lines can be created (e.g. **2l**, **3l**, **4l**), and they are on different mirror planes, intersecting each other at \mathbf{k}_0 .

In the following, we explain how these patterns emerge for various \mathbf{k} points in 138 space groups without inversion symmetry. Time-reversal symmetry is assumed throughout. All the cases are classified in terms of space groups and values of \mathbf{k}_0 where the gap closes. Then, various cases for each \mathbf{k} point are classified in terms of irreducible representation of the conduction band and that of the valence band, denoted as R_c and R_v , respectively. As explained in the main text, we have to study only the cases with $\dim R_c = \dim R_v = 1$ because otherwise the gap cannot close \mathbf{k}_0 . In particular, one can exclude the TRIM as \mathbf{k}_0 , since there is always Kramers degeneracy at the TRIM, and the gap cannot close. In addition, if a high-symmetry point shares the same k -group with a high-symmetry line which includes this point, the gap does not close at the high-symmetry point, because it requires fine-tuning of the Hamiltonian.

In the following tables, we show the high-symmetry points and lines, where the gap can close by changing a single parameter m . It should be noted that in addition to the patterns listed in the following tables, the following two patterns exist, which are common to all the space groups.

- generic \mathbf{k} without any symmetry: **1** (the case (i) in the main text)
- generic \mathbf{k} on a mirror plane: **1sa** for $R_c = R_v$ (the case (iv-1)), and **1l**, for $R_c \neq R_v$ (the case (iv-2)). In the

former case, the conduction and valence bands have the same signs of mirror eigenvalues, while in the latter, they have the opposite signs.

In the following tables S1-S5, we show all the patterns for the combinations of R_c and R_v , where the gap can close by changing the parameter m . Cases where the gap cannot close at \mathbf{k}_0 are excluded from the tables. We show all the 138 space groups without inversion symmetry. In the tables “point” and “line” refer to the high-symmetry points and the high-symmetry lines, respectively. As noted above, R_c and R_v should be both one-dimensional. The names of the irreducible representations (irreps) follows the notation in Ref. S1, such as R_1 and R_2 , and so on. For a concise expression in the tables, we use the symbols “ii” and “ij”; “ii” means the case with $R_c = R_v$ and “ij” means the case with $R_c \neq R_v$, respectively. When there is only one representation allowed for the \mathbf{k} point, such symbols are not needed and thus are not shown. For more complicated cases, for example, the entry (3, 4) in the tables means $(R_c, R_v) = (R_3, R_4), (R_4, R_3)$. Furthermore, some lengthy entities are abbreviated in the following way:

$\langle 1 \rangle = (R_2, R_3)(R_4, R_5); \mathbf{2l}, (R_2, R_4)(R_3, R_5)(R_2, R_5)(R_3, R_4); \mathbf{1l}.$
 $\langle 2 \rangle = (R_5, R_6)(R_6, R_7)(R_7, R_8)(R_8, R_5); \mathbf{1sa}, (R_5, R_7)(R_6, R_8); \mathbf{2sp}.$
 $\langle 3 \rangle = (R_2, R_5)(R_3, R_4); \mathbf{2l}, (R_2, R_3)(R_4, R_5)(R_2, R_4)(R_3, R_5); \mathbf{1l}.$
 $\langle 4 \rangle = (R_5, R_6)(R_6, R_7)(R_7, R_8)(R_8, R_5); \mathbf{1sa}, (R_5, R_7)(R_6, R_8); \mathbf{2sa}.$
 $\langle 5 \rangle = (R_3, R_4)(R_5, R_6); \mathbf{2l}, (R_3, R_5)(R_4, R_6); \mathbf{2sca}, (R_3, R_6)(R_4, R_5); \mathbf{1l}.$
 $\langle 6 \rangle = (R_{11}, R_8)(R_{10}, R_9)(R_7, R_{12}); \mathbf{1l}, (R_{11}, R_7)(R_{10}, R_8)(R_7, R_9)(R_8, R_{12})(R_9, R_{11})(R_{12}, R_{10}); \mathbf{1sa}, (R_{11}, R_{10})(R_{10}, R_7)(R_7, R_8)(R_8, R_9)(R_9, R_{12})(R_{12}, R_{11}); \mathbf{1sa1l}.$
 $\langle 7 \rangle = (R_4, R_5)(R_5, R_6)(R_6, R_4); \mathbf{4st}.$
 $\langle 8 \rangle = (R_4, R_7)(R_5, R_6); \mathbf{4l}, (R_4, R_5)(R_6, R_7); \mathbf{3l}, (R_4, R_6)(R_5, R_7); \mathbf{1l}.$

space group	point	line
1 $P1$		
3 $P2$		$\Delta V W U:ij;\mathbf{1a}$
4 $P2_1$		$\Delta V W U:ij;\mathbf{1a}$
5 $C2$		$\Delta U:ij;\mathbf{1a}$
6 Pm		$\Delta V W U:\mathbf{1sp}$
7 Pc		$\Delta W:\mathbf{1sp}$
8 Cm		$\Delta U:\mathbf{1sp}$
9 Cc		$\Delta:\mathbf{1sp}$

TABLE S1. Patterns of gap-closing points after parametric gap closing for triclinic and monoclinic space groups.

PROPERTIES OF BAND STRUCTURE OF HfS

Here we briefly explain the band structure of HfS and the reason why it is appropriate as a candidate for a nodal-line semimetal. The crystal structure of HfS is the same as that of tungsten carbide (WC). Its space group is No. 187 ($P6m2$) [S2], and it has several mirror planes, which are necessary for the Weyl nodal lines by mirror symmetry as we discussed. Bands of the Hf $5d$ orbitals are classified into three

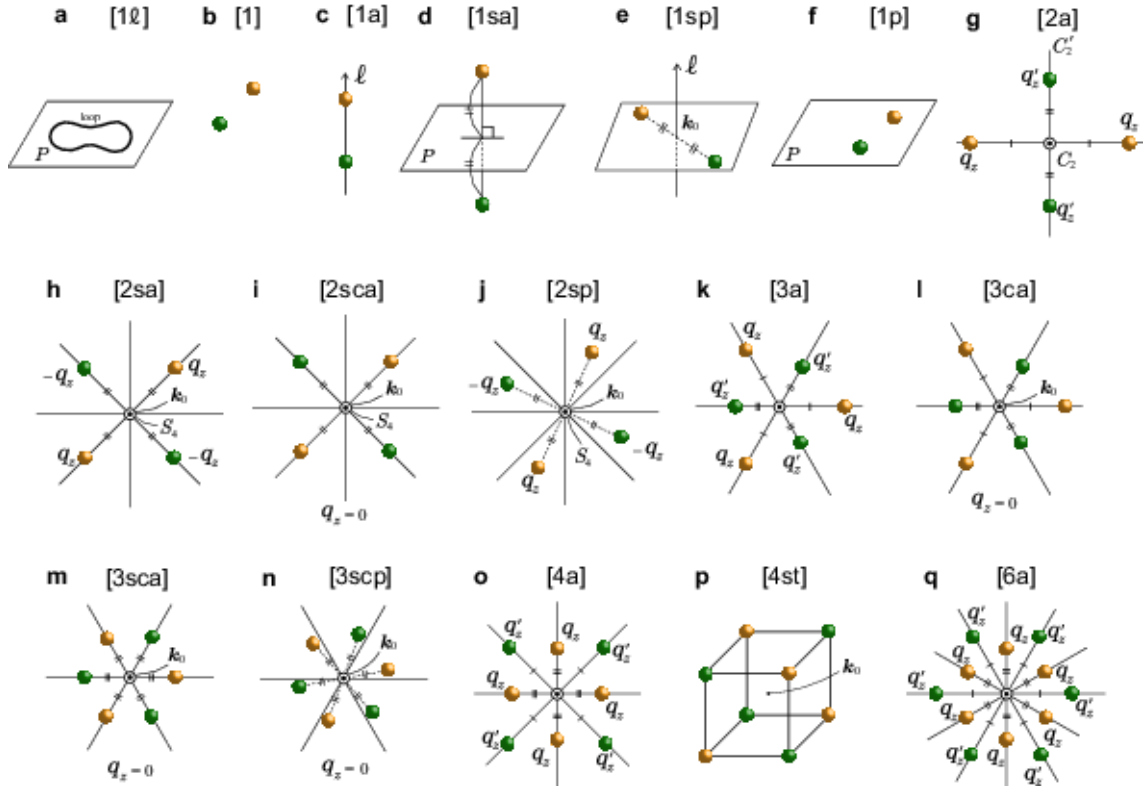


FIG. S2. All the patterns of gap-closing points after parametric gap closing. **a**, Line nodes for a nodal-line semimetal. It shows a single line node, whereas the number of line nodes can range among 1, 2, 3, 4 and 6. **b-q**, All the pattern of Weyl nodes after parametric gap closing at \mathbf{k}_0 . Yellow and green spheres denote monopoles and antimonopoles in \mathbf{k} space, respectively, and they are both Weyl nodes. Solid lines denote high-symmetry directions. The z axis is parallel to a high-symmetry axis which is taken to be perpendicular to the page, and $\mathbf{q} \equiv \mathbf{k} - \mathbf{k}_0$ is the momentum measured from \mathbf{k}_0 . In **i**, **l**, **m** and **n**, all the Weyl nodes are coplanar with \mathbf{k}_0 , while in **g**, **h**, **j**, **k**, **o**, and **q**, the Weyl nodes are mutually displaced along the z direction.

groups, a'_1 , e' , and e'' , by the crystal field from a trigonal prism of S^{2+} atoms. A narrow gap is formed between the occupied a'_1 band and the unoccupied e' bands. A layered triangle lattice formed by Hf atoms is favorable for displacing the point of the minimum band gap away from the Γ point to the K point by interference effects. When the spin-orbit coupling (SOC) is neglected, Dirac nodal-line exists around the K point on the $k_z = 0$ plane.

When the SOC is considered, due to mismatch between threefold rotational symmetry of the trigonal prism and the right angle of electronic clouds of atomic d orbitals, wave-functions become necessarily complex, and a relativistic energy splitting would be partially enhanced. Spin splitting vanishes at the TRIM, while it is prominent at the non-TRIM points such as K- and H-points. Thus the SOC lifts the degeneracy in the Dirac nodal-line, and the Weyl nodal-line appears instead near the K point on the mirror plane $k_z = 0$.

[S2] Franzen, H. F. & Graham, J. J. The lower sulphides of hafnium at high temperature. *J. Inorg. Nucl. Chem.* **28**, 377 (1966).

[S1] Bradley, C. J., & Cracknell, A. P. *The Mathematical Theory of Symmetry in Solids: Representation Theory for Point Groups and Space Groups* (Oxford Univ Press, Oxford, 2010).

space group	point	line
16 $P222$		$\Delta DPB\bar{\Sigma}CEA\Delta HQG:ii;2a,ij;1a$
17 $P222_1$		$\Delta D\bar{\Sigma}CAHQG:ii;2a,ij;1a$
18 $P2_12_12$		$\Delta B\bar{\Sigma}A\Delta:ii;2a,ij;1a$
19 $P2_12_12_1$		$\Delta \Sigma\Delta:ii;2a,ij;1a$
20 $C222_1$		$\Delta H\bar{\Sigma}\Delta FC:ii;2a,ij;1a D:ij;1a$
21 $C222$		$\Delta H\bar{\Sigma}\Delta BG\bar{F}EC:ii;2a,ij;1a D:ij;1a$
22 $F222$		$\Delta GHQ\bar{\Sigma}CAU\Delta DBR:ii;2a,ij;1a$
23 $I222$		$\Delta G\bar{\Sigma}FAU:ii;2a,ij;1a PDQ:ij;1a$
24 $I2_12_12_1$	W:ij;2a	$\Delta G\bar{\Sigma}FAU:ii;2a,ij;1a PDQ:ij;1a$
25 $Pmm2$		$\Delta DPB\bar{\Sigma}CEA:ii;1sa,ij;1\ell$
26 $Pmc2_1$		$\Delta D\bar{\Sigma}C:ii;1sa,ij;1\ell$
27 $Pcc2$		$\Delta D\bar{\Sigma}C:ii;1sa,ij;1\ell$
28 $Pma2$		$\Delta DPB\bar{\Sigma}A:ii;1sa,ij;1\ell HQ:(1)$
29 $Pca2_1$		$\Delta D\bar{\Sigma}:ii;1sa,ij;1\ell HQ:(1)$
30 $Pnc2$		$\Delta D\bar{\Sigma}E:ii;1sa,ij;1\ell HQ:(1)$
31 $Pmn2_1$		$\Delta D\bar{\Sigma}:ii;1sa,ij;1\ell HQ:(1)$
32 $Pba2$		$\Delta B\bar{\Sigma}A:ii;1sa,ij;1\ell HG:(1)$
33 $Pna2_1$		$\Delta \Sigma:ii;1sa,ij;1\ell HG:(1)$
34 $Pnn2$		$\Delta P\bar{\Sigma}E:ii;1sa,ij;1\ell HG:(1)$
35 $Cmm2$		$D:ij;1a \Delta \bar{\Sigma}BG\bar{F}EC:ii;1sa,ij;1\ell$
36 $Cmc2_1$		$D:ij;1a \Sigma \Delta FC:ii;1sa,ij;1\ell$
37 $Ccc2$		$D:ij;1a \Sigma \Delta FC:ii;1sa,ij;1\ell$
38 $Amm2$		$\Delta H\bar{\Sigma}E\bar{C}:ii;1sa,ij;1\ell D:1sp$
39 $Aem2$		$\Delta H\bar{\Sigma}E\bar{C}:ii;1sa,ij;1\ell$
40 $Ama2$		$\Delta H\bar{\Sigma}C:ii;1sa,ij;1\ell D:1sp BG:(3)$
41 $Aea2$		$\Delta H\bar{\Sigma}C:ii;1sa,ij;1\ell BG:(3)$
42 $Fmm2$		$\Sigma CAU\Delta DBR:ii;1sa,ij;1\ell$
43 $Fdd2$		$\Sigma U\Delta R:ii;1sa,ij;1\ell GH:(1)$
44 $Imm2$	W:ij;1sa	$P:ij;1a \Sigma F\Delta U:ii;1sa,ij;1\ell DQ:1sp$
45 $Iba2$		$P:ij;1a \Sigma F\Delta U:ii;1sa,ij;1\ell$
46 $Ima2$		$P:ij;1a \Sigma F\Delta U:ii;1sa,ij;1\ell Q:1sp$

TABLE S2. Patterns of gap-closing points after parametric gap closing for orthorhombic space groups. We note that in No38, 39, 40 and 41, despite the space group symbols use the A lattice for orthorhombic base-centered Bravais lattice, we use the C lattice with the twofold rotation axis is along y , following the notations in Ref. S1 (see p.83 and p135 in Ref. S1)

space group	point	line
75 $P4$		$\Delta U\bar{\Sigma}SYT:1p \Delta VW:ij;1a$
76 $P4_1$		$\Delta \Sigma Y:1p \Delta VW:ij;1a$
77 $P4_2$		$\Delta U\bar{\Sigma}SYT:1p \Delta VW:ij;1a$
78 $P4_3$		$\Delta \Sigma Y:1p \Delta VW:ij;1a$
79 $I4$		$\Delta VW:ij;1a \Sigma F\Delta UY:1p$
80 $I4_1$		$\Delta VW:ij;1a \Sigma F\Delta UY:1p$
81 $P\bar{4}$		$\Delta U\bar{\Sigma}SYT:1p W:ij;1a$
82 $\bar{I}4$	P:(2)	$W:ij;1a \Sigma F\Delta UY:1p$
89 $P422$		$\Delta U\bar{\Sigma}SYTW:ii;2a,ij;1a \Delta V:ii;4a,ij;1a$
90 $P42_12$		$\Delta U\bar{\Sigma}:ii;2a,ij;1a \Delta:ii;4a,ij;1a$
91 $P4_122$		$\Delta \Sigma YW:ii;2a,ij;1a \Delta V:ii;4a,ij;1a$
92 $P4_12_12$		$\Delta \Sigma:ii;2a,ij;1a \Delta:ii;4a,ij;1a$
93 $P4_222$		$\Delta U\bar{\Sigma}SYTW:ii;2a,ij;1a \Delta V:ii;4a,ij;1a$
94 $P4_22_12$		$\Delta U\bar{\Sigma}:ii;2a,ij;1a \Delta:ii;4a,ij;1a$
95 $P4_322$		$\Delta \Sigma YW:ii;2a,ij;1a \Delta V:ii;4a,ij;1a$
96 $P4_32_12$		$\Delta \Sigma:ii;2a,ij;1a \Delta:ii;4a,ij;1a$
97 $I422$		$\Delta V:ii;4a,ij;1a W\bar{\Sigma}F\Delta UY:ii;2a,ij;1a Q:ij;1a$
98 $I4_122$	P:(2,3);4a	$\Delta V:ii;4a,ij;1a W\bar{\Sigma}F\Delta UY:ii;2a,ij;1a Q:ij;1a$
99 $P4mm$		$\Delta U\bar{\Sigma}SYT:ii;1sa,ij;1\ell$
100 $P4bm$		$\Delta U\bar{\Sigma}:ii;1sa,ij;1\ell W:(3)$
101 $P4_2cm$		$\Delta \Sigma Y:ii;1sa,ij;1\ell$
102 $P4_2nm$		$\Delta \Sigma ST:ii;1sa,ij;1\ell W:(3)$
103 $P4cc$		$\Delta \Sigma Y:ii;1sa,ij;1\ell$
104 $P4nc$		$\Delta \Sigma T:ii;1sa,ij;1\ell W:(3)$
105 $P4_2mc$		$\Delta U\bar{\Sigma}YT:ii;1sa,ij;1\ell$
106 $P4_2bc$		$\Delta U\bar{\Sigma}:ii;1sa,ij;1\ell W:(3)$
107 $I4mm$		$\Sigma F\Delta UY:ii;1sa,ij;1\ell Q:1sp$
108 $I4cm$		$\Sigma F\Delta UY:ii;1sa,ij;1\ell$
109 $I4_1md$	P:(13,14);2\ell	$W:(3) \Sigma F\Delta:ii;1sa,ij;1\ell Q:1sp$
110 $I4_1cd$		$W:(3) \Sigma F\Delta:ii;1sa,ij;1\ell$
111 $P\bar{4}2m$		$\Delta UYT\bar{W}:ii;2a,ij;1a \Sigma S:ii;1sa,ij;1\ell$
112 $P\bar{4}2c$		$\Delta UYT\bar{W}:ii;2a,ij;1a \Sigma:ii;1sa,ij;1\ell$
113 $P\bar{4}2_1m$		$\Delta U:ii;2a,ij;1a \Sigma S:ii;1sa,ij;1\ell$
114 $P\bar{4}2_1c$		$\Delta U:ii;2a,ij;1a \Sigma:ii;1sa,ij;1\ell$
115 $P4m2$		$\Delta UYT:ii;1sa,ij;1\ell \Sigma S:ii;2a,ij;1a$
116 $P\bar{4}c2$		$\Delta Y:ii;1sa,ij;1\ell \Sigma S:ii;2a,ij;1a$
117 $P\bar{4}b2$		$\Delta U:ii;1sa,ij;1\ell \Sigma S:ii;2a,ij;1a W:(3)$
118 $P\bar{4}n2$		$\Delta T:ii;1sa,ij;1\ell \Sigma S:ii;2a,ij;1a W:(3)$
119 $I\bar{4}m2$	P:(4)	$W\Delta UY:ii;2a,ij;1a \Sigma F:ii;1sa,ij;1\ell Q:1sp$
120 $\bar{I}4c2$		$W\Delta UY:ii;2a,ij;1a \Sigma F:ii;1sa,ij;1\ell$
121 $\bar{I}42m$		$\Sigma F:ii;2a,ij;1a Q:ij;1a \Delta UY:ii;1sa,ij;1\ell$
122 $\bar{I}42d$	P:(5)	$W:(3) \Sigma F:ii;2a,ij;1a \Delta:ii;1sa,ij;1\ell Q:ij;1a$

TABLE S3. Patterns of gap-closing points after parametric gap closing for tetragonal space groups.

space group	point	line
143 $P3$		$\Delta P:ij;1a$
144 $P3_1$		$\Delta P:ij;1a$
145 $P3_2$		$\Delta P:ij;1a$
146 $R3$		$\Delta P:ij;1a$
149 $P3_{12}$		$\Delta P:ii;3a,ij;1a$ $UTST'S':1p$ $\Sigma R:ij;1a$
150 $P3_{21}$	$KH:(3,4);3ca$	$\Delta:ii;3a,ij;1a$ $U\Sigma R:1p$ $PTST'S':ij;1a$
151 $P3_1 12$		$\Delta P:ii;3a,ij;1a$ $UTST'S':1p$ $\Sigma R:ij;1a$
152 $P3_1 21$	$KH:(3,4);3ca$	$\Delta:ii;3a,ij;1a$ $U\Sigma R:1p$ $PTST'S':ij;1a$
153 $P3_2 12$		$\Delta P:ii;3a,ij;1a$ $UTST'S':1p$ $\Sigma R:ij;1a$
154 $P3_2 21$	$KH:(3,4);3ca$	$\Delta:ii;3a,ij;1a$ $U\Sigma R:1p$ $PTST'S':ij;1a$
155 $R32$		$\Delta P:ij;3a,ij;1a$ $B\Sigma QY:ij;1a$
156 $P3m1$	$KH:ij;1a$	$\Delta:(3,4);3\ell$ $U\Sigma R:ij;1\ell$ $P:ij;1a$ $TST'S':1sp$
157 $P31m$		$\Delta P:(3,4);3\ell$ $UTST'S':ij;1\ell$ $\Sigma R:1sp$
158 $P3c1$	$K:ij;1a$	$\Delta:(3,4);3\ell$ $P:ij;1a$ $U\Sigma R:ij;1\ell$ $TT':1sp$
159 $P31c$		$\Delta P:(3,4);3\ell$ $UTST'S':ij;1\ell$ $\Sigma:1sp$
160 $R3m$		$\Delta P:(3,4);3\ell$ $B\Sigma QY:1sp$
161 $R3c$		$\Delta P:(3,4);3\ell$ $\Sigma Q:1sp$
168 $P6$		$\Delta UP:ij;1a$ $TST'S'\Sigma R:1p$
169 $P6_1$		$\Delta UP:ij;1a$ $TT'\Sigma:1p$
170 $P6_5$		$\Delta UP:ij;1a$ $TT'\Sigma:1p$
171 $P6_2$		$\Delta UP:ij;1a$ $TST'S'\Sigma R:1p$
172 $P6_4$		$\Delta UP:ij;1a$ $TST'S'\Sigma R:1p$
173 $P6_3$		$\Delta UP:ij;1a$ $TT'\Sigma:1p$
174 $P\bar{6}$	$KH:(6)$	$\Delta:(4,4);3scp$ $U:1sp$ $P:ij;1a$ $TST'S'\Sigma R:ij;1\ell$
177 $P6_{22}$	$KH:(3,4);3ca$	$\Delta:ii;6a,ij;1a$ $UTST'S'\Sigma R:ii;2a,ij;1a$ $P:ii;3a,ij;1a$
178 $P6_1 22$	$K:(3,4);3ca$	$\Delta:ii;6a,ij;1a$ $UTT'\Sigma:ii;2a,ij;1a$ $P:ii;3a,ij;1a$
179 $P6_5 22$	$K:(3,4);3ca$	$\Delta:ii;6a,ij;1a$ $UTT'\Sigma:ii;2a,ij;1a$ $P:ii;3a,ij;1a$
180 $P6_2 22$	$KH:(3,4);3ca$	$\Delta:ii;6a,ij;1a$ $UTST'S'\Sigma R:ii;2a,ij;1a$ $P:ii;3a,ij;1a$
181 $P6_4 22$	$KH:(3,4);3ca$	$\Delta:ii;6a,ij;1a$ $UTST'S'\Sigma R:ii;2a,ij;1a$ $P:ii;3a,ij;1a$
182 $P6_3 22$	$K:(3,4);3ca$	$\Delta:ii;6a,ij;1a$ $UTT'\Sigma:ii;2a,ij;1a$ $P:ii;3a,ij;1a$
183 $P6mm$	$KH:(3,4);3\ell$	$P:(3,4);3\ell$ $TST'S'\Sigma R:ii;1sa,ij;1\ell$
184 $P6cc$	$K:(3,4);3\ell$	$P:(3,4);3\ell$ $TT'\Sigma:ii;1sa,ij;1\ell$
185 $P6_3 cm$	$K:(3,4);3\ell$	$P:(3,4);3\ell$ $TT'\Sigma:ii;1sa,ij;1\ell$
186 $P6_3 mc$	$K:(3,4);3\ell$	$P:(3,4);3\ell$ $TT'\Sigma:ii;1sa,ij;1\ell$
187 $P\bar{6}m2$	$KH:(6)$	$\Delta:(3,4);3\ell$ $(3,3)(4,4);3sca$ $UTST'S':ii;1sa,ij;1\ell$ $P:ii;3a,ij;1a$
188 $P\bar{6}c2$	$K:(6)$	$\Delta:(3,4);3\ell$ $(3,3)(4,4);3sca$ $UTT':ii;1sa,ij;1\ell$ $P:ii;3a,ij;1a$ $R:(1)$
189 $P\bar{6}2m$		$\Delta:(3,4);3\ell$ $(3,3)(4,4);3sca$ $U\Sigma R:ii;1sa,ij;1\ell$ $P:(3,4);3\ell$
190 $P\bar{6}2c$	$H:(8)$	$\Delta:(3,4);3\ell$ $(3,3)(4,4);3sca$ $U\Sigma:ii;1sa,ij;1\ell$ $P:(3,4);3\ell$ $SS':(1)$

TABLE S4. Patterns of gap-closing points after parametric gap closing for trigonal and hexagonal space groups.

space group	point	line
195 $P23$		$\Delta ZT:ii;2a,ij;1a$ $\Sigma S:1p$ $\Lambda:ij;1a$
196 $F23$	$W:ij;1a$	$\Delta Z:ii;2a,ij;1a$ $\Lambda:ij;1a$ $\Sigma S:1p$
197 $I23$		$\Sigma G:1p$ $\Delta:ii;2a,ij;1a$ $\Lambda DF:ij;1a$
198 $P2_1 3$		$\Delta:ii;2a,ij;1a$ $\Sigma:1p$ $\Lambda:ij;1a$
199 $I2_1 3$	$P:(7)$	$\Sigma G:1p$ $\Delta:ii;2a,ij;1a$ $\Lambda DF:ij;1a$
207 $P432$		$\Delta T:ii;4a,ij;1a$ $\Sigma SZ:ii;2a,ij;1a$ $\Lambda:ii;3a,ij;1a$
208 $P4_2 32$		$\Delta T:ii;4a,ij;1a$ $\Sigma SZ:ii;2a,ij;1a$ $\Lambda:ii;3a,ij;1a$
209 $F432$		$\Delta:ii;4a,ij;1a$ $\Lambda:ii;3a,ij;1a$ $\Sigma SZ:ii;2a,ij;1a$ $Q:ij;1a$
210 $F4_1 32$	$W:(2,4);4a$	$\Delta:ii;4a,ij;1a$ $\Lambda:ii;3a,ij;1a$ $\Sigma SZ:ii;2a,ij;1a$ $Q:ij;1a$
211 $I432$		$\Sigma DG:ii;2a,ij;1a$ $\Delta:ii;4a,ij;1a$ $\Lambda F:ii;3a,ij;1a$
212 $P4_3 32$		$\Delta:ii;4a,ij;1a$ $\Sigma:ii;2a,ij;1a$ $\Lambda:ii;3a,ij;1a$
213 $P4_1 32$		$\Delta:ii;4a,ij;1a$ $\Sigma:ii;2a,ij;1a$ $\Lambda:ii;3a,ij;1a$
214 $I4_1 32$	$P:(7)$	$\Sigma DG:ii;2a,ij;1a$ $\Delta:ii;4a,ij;1a$ $\Lambda F:ii;3a,ij;1a$
215 $P\bar{4}3m$		$\Sigma S:ii;1sa,ij;1\ell$ $\Lambda:(3,4);3\ell$ $Z:ii;2a,ij;1a$
216 $F\bar{4}3m$	$W:(4)$	$\Lambda:(3,4);3\ell$ $\Sigma S:ii;1sa,ij;1\ell$ $Z:ii;2a,ij;1a$ $Q:1sp$
217 $I\bar{4}3m$		$\Sigma G:ii;1sa,ij;1\ell$ $\Lambda(3,4);3\ell$
218 $P\bar{4}3n$		$\Sigma:ii;1sa,ij;1\ell$ $\Lambda:(3,4);3\ell$ $Z:ii;2a,ij;1a$
219 $F\bar{4}3c$		$\Lambda:(3,4);3\ell$ $\Sigma S:ii;1sp,ij;1\ell$ $Z:ii;2a,ij;1a$
220 $I\bar{4}3d$	$P:(17,18);6\ell$	$\Sigma:ii;1sa,ij;1\ell$ $\Lambda:(3,4);3\ell$ $D:(1)$ $F:(9,10);3\ell$

TABLE S5. Patterns of gap-closing points after parametric gap closing for cubic space groups.